20. Wojnarowski J., Mirota K., Własności reologiczne krwi ludzkiej w modelowaniu opływu sztucznej zastawki (*XXX Sympozjon Modelowanie w Mechanice*, Wisła-Gliwice 1996) pp. 251-256.
21. Hoppensteadt C.F., Peskin C.S., *Mathematics in medicine and the life sciences*, (Springer Verlag, New York 1992).

THERMOMECHANICS OF BONE-IMPLANT INTERFACES AFTER CEMENTED JOINT ARTHROPLASTY : THEORETICAL MODELS AND COMPUTATIONAL ASPECTS

LALAONIRINA R. RAKOTOMANANA
Institut de Recherche Mathématiques de Rennes
UMR 6625 CNRS - Université de Rennes 1, 35 042 Rennes, France
E-mail: lalaonirina.rakotomanana@univ-rennes1.fr

NIRINA A. RAMANIRAKA
Centre de Recherche Orthopédique, EPF Lausanne, Suisse

Numerous factors are known to influence the fixation of orthopedic implants, such as the bone quality, the implant design and the bone-implant interface. Accurate evaluation of the bone-implant micromotion and interfacial stress is a keystone for determining the mechanical environment acting on the surrounding bone tissue and cells. This work presents some theoretical models and computational methods to investigate the initial fixation of orthopedic implants. Both mechanical and thermal aspects are considered. A cemented femoral component was chosen to illustrate the developed models.

1 Introduction

After joint arthroplasty, failure of cemented implants is commonly related to wear particles resulting from cement fracture and fragmentation due to high stress and enhanced by a migration of debris particles along cement-bone interface. More specifically, after cemented Total Hip Replacement, failures at stem-cement interface and at bone-cement interface mainly resulted from the occurrence of abnormally high cement stresses and excessive micromotions [1,2]. High compressive stress was source of cement fracture and enhanced the stem subsidence while excessive slipping enhanced the creation of cement debris. Bone-cement slipping leaded to a necrosis of bone that interdigitize with the cement. Interfaces roughness strongly influenced the stress and micromotions. Improving the cement-stem bonding increased stress at cement-bone interface [2]. The cement thickness was another factor influencing sensibly stress magnitude, observed either clinically or experimentally [3]. Mechanical and thermal problems at the interface are very sensitive to minor changes of contacting boundaries of the bone, cement and implants. This sensitivity is increased by thermoelastic distortion [4]. It may have important consequence of the long term reliability of the implant anchorage, particularly on the generation of microcraks within the cement mantle. Some biological complications

might be related to the heat generated by the exothermic polymerization of the orthopaedic cement. Bone necrosis at the bone-cement interface may occur during and after the surgical implantation. This may induce bone resorption at the bone-cement interface, leading implant lose. A brief review allows to cite some variables which may affect the interface behaviour: micromotions and stresses, wear and debris at the bone-cement and cement-stem interfaces, bone remodeling and formation of fibrous tissue, and thermal effects due to cement and to frictional contact at the interface.

Computational techniques are more and more used to calculate these mechanical and thermal variables trying to simulate clinical situations [5]. However, coupling of all of these variables drastically increases the problem difficulty. To name but several, stem temperature, cement temperature, polymerization temperature, thermoelastic properties of bone, cement and stem including the shrinkage stresses of the cement [6], certainly affect the quality of the anchorage either immediatly after operation or in the long term. As a starting point, accurate calculation of the bone-implant relative micromotions and interfacial stresses becomes a keypoint for any quantitative analysis of the mechanical environment acting on the bone tissue and cells. Some numerical algorithms are also very sensitive to solution parameters [7] and it is always reasonable to question about exactness of theoretical models and efficiency of numerical computations.

The purpose of this work was to present theoretical models and computational methods to analyse the fixation of orthopedic implants. Only some thermomechanics aspects are considered. This paper focuses on the development of theoretical models for interface thermomechanics, and of numerical algorithms with application to cemented arthroplasty.

2 Thermomechanics of the Interface

2.1 Interface thermokinematics

Interface kinematics includes cohesion-decohesion and adherence and sliding between the contacting surfaces. We limit to infinitesimal deformation within body and infinitesimal relative displacement at the interface. Considering two deformable bodies B and B'. B is limited by the boundary $\partial B = \partial B_p \cup \partial B_c \cup \partial B_u$, where on ∂B_u displacement is imposed, on ∂B_p stress vector is imposed, and ∂B_c is the contact surface between B and B'. The same decomposition holds for B' (see Fig. 1). B' is called the target and B the striker. For any point $M \in \partial B_c$, the proximal point $M^\perp$ the position of which $\mathbf{OM}^\perp = \varphi'(M^\perp, t)$ is the nearest of that to M [8]:

$$\mathbf{OM}^\perp = \operatorname{argmin}\left[\frac{1}{2}\|\varphi(M,t) - \varphi'(M',t)\|^2\right]_{M' \in \partial B'_c} \tag{1}$$

The gap vector $\mathbf{d}$ is defined by [8] $\mathbf{d} \equiv \varphi(M,t) - \varphi'(M^\perp,t) = \mathbf{M}^\perp\mathbf{M}$ where $\mathbf{OM}^\perp(M,t)$. The normal gap vector d_n is the component of $\mathbf{d}$ along $\mathbf{n}'(M^\perp,t)$, normal at $M^\perp$ (normal micromotions):

$$d_n(M,t) \equiv \mathbf{n}'(M^\perp,t) \cdot [\varphi(M,t) - \varphi'(M^\perp,t)] \tag{2}$$

Three situations may occur: $d_n > 0$ gap, $d_n = 0$ contact and $d_n < 0$ penetration. The slipping vector (shear micromotions) is then given by:

$$\mathbf{d}_T(M,t) \equiv \mathbf{d}(M,t) - d_n(M,t)\mathbf{n}'(M^\perp,t) \tag{3}$$

The rate of the gap vector is the relative velocity of M located in $\varphi(M,t) \in \partial B_c$, with respect to $M^\perp$, located in $\varphi'(M^\perp,t) \in \partial B'_c$. :

$$\dot{\mathbf{d}} = \frac{d}{dt}\varphi(M,t) - \frac{d}{dt}\varphi'(M^\perp,t) \tag{4}$$

It is not frame indifferent unless the normal gap vanishes. However, for small relative displacements, there is no need to introduce objective relative velocity. Normal and tangential projections of $\dot{\mathbf{d}}$ are respectively:

$$\begin{aligned}\dot{\mathbf{d}}_n &= \left[\mathbf{n}'(M^\perp,t) \otimes \mathbf{n}'(M^\perp,t)\right]\ \dot{\mathbf{d}}(M,M^\perp,t)\\ \dot{\mathbf{d}}_T &= \left[\mathbb{I} - \mathbf{n}'(M^\perp,t) \otimes \mathbf{n}'(M^\perp,t)\right]\ \dot{\mathbf{d}}(M,M^\perp,t)\end{aligned} \tag{5}$$

By analogy with $\mathbf{d}$, we define the temperature-gap $\delta\theta$ and its rate:

$$\delta\theta = \delta\theta(M,t) = \theta(M,t) - \theta'(M^\perp(M,t),t) \qquad \dot{\delta\theta} = \frac{d\delta\theta}{dt} \tag{6}$$

2.2 Conservation laws at the interface

Interface thermomechanics can be described by the position $\mathbf{OM}(t)$ and contact gap $\mathbf{d}(M,t)$; the absolute temperature $\theta(M,t)$ and temperature gap $\delta\theta(M,t)$; the contact stress vectors $\mathbf{p}(M,t)$ and $\mathbf{p}'(M',t)$; the entropy $s(M,t)$ and interfacial entropy $s_c(M,t)$; the internal energy $e(M,t)$ and interfacial energy $e_c(M,t)$; the contact heat fluxes $q(M,t)$, $q'(M',t)$; the body force $\rho\mathbf{b}(M,t)$ and volume heat source $r(M,t)$ [9].

Let $\mathcal{A}$ be the quantity which varies within $\Sigma = B \cup B'$ and $\mathcal{B}$ the volume production and $\mathcal{C}(\partial\Sigma,t)$ the flux exchange with the external environment. The generic conservation law holds:

$$\frac{d}{dt}\mathcal{A}(\Sigma,t) \geqq \mathcal{B}(\Sigma,t) + \mathcal{C}(\partial\Sigma,t). \tag{7}$$

Any subsystem of Σ must satisfy (7). When B and B' shrink down respectively to ∂B_c and $\partial B'_c$, their volume vanishes while the areas of the contact surfaces remain finite. Two situations may occur: (a) *no contact* the target surface and the striker surface are empty sets, (b) *contact* there is a bijective map between the two contacting surfaces.

1. **For linear momentum.** We introduce:

$$\mathcal{A}(\Sigma,t) = \int_B \rho \mathbf{v} dv + \int_{B'} \rho' \mathbf{v}' dv' \tag{8}$$

$$\mathcal{B}(\Sigma,t) = \int_B \rho \mathbf{b} dv + \int_{B'} \rho' \mathbf{b}' dv' \tag{9}$$

$$\mathcal{C}(\partial\Sigma,t) = \int_{\partial B} \mathbf{p}_n da + \int_{\partial B'} \mathbf{p}'_n da' \tag{10}$$

Since this relation must be satisfied for any subsystem of Σ, we obtain the three equations for any point of B, B', and $\partial B_c \cap \partial B'_c$ respectively:

$$\begin{aligned} \rho \dot{\mathbf{v}}(M,t) &= \rho \mathbf{b}(M,t) + \mathrm{div}\sigma(M,t) \\ \rho' \dot{\mathbf{v}}'(M',t) &= \rho' \mathbf{b}'(M',t) + \mathrm{div}\sigma'(M',t) \\ \mathbf{p}(M,t) + \mathbf{p}'(M^{\perp}(M,t),t) &= 0 \end{aligned} \tag{11}$$

2. **For angular momentum.** Consider the angular momentum with respect to any fixed point O. We introduce:

$$\mathcal{A}(\Sigma,t) = \int_B \mathbf{OM} \times \rho \mathbf{v} dv + \int_{B'} \mathbf{OM}' \times \rho' \mathbf{v}' dv' \tag{12}$$

$$\mathcal{B}(\Sigma,t) = \int_B \mathbf{OM} \times \rho \mathbf{b} dv + \int_{B'} \mathbf{OM}' \times \rho' \mathbf{b}' dv' \tag{13}$$

$$\mathcal{C}(\partial\Sigma,t) = \int_{\partial B} \mathbf{OM} \times \mathbf{p} da + \; + \int_{\partial B'} \mathbf{OM}' \times \mathbf{p}' da' \tag{14}$$

Application of this general relation for any subsystem of Σ induces the three equations for any point of B, B', and $\partial B_c \cap \partial B'_c$ respectively:

$$\begin{aligned} \sigma(M,t) = \sigma^T(M,t) \quad \sigma'(M',t) = \sigma'^T(M',t) \\ \mathbf{MM}^{\perp}(M,t) \times \mathbf{p} = 0 \end{aligned} \tag{15}$$

3. **For internal energy.** For the energy, $\mathcal{A}(\Sigma,t)$ includes the kinetic $\mathcal{K}(\Sigma,t)$ and internal energy $\mathcal{E}(\Sigma,t)$. This later is not additive:

$$\dot{\mathcal{E}}(\Sigma,t) = \dot{\mathcal{E}}(B,t) + \dot{\mathcal{E}}'(B',t) + \int_{\partial B_c} \frac{de_c}{dt} da \tag{16}$$

in which the third term of the right side represents the interfacial energy between B and B'. We thus define the kinetic energy, internal energy, power of external forces, and volume and heat fluxes respectively:

$$\mathcal{K}(\Sigma,t) = \frac{1}{2}\int_B \rho \mathbf{v}^2 dv + \int_{B'} + \frac{1}{2}\int_{B'} \rho' \mathbf{v}'^2 dv' \tag{17}$$

$$\mathcal{E}(\Sigma,t) = \int_B \rho e dv + \int_{B'} \rho' e' dv' + \mathcal{E}(B \cap B', t) \tag{18}$$

$$\begin{aligned} \mathcal{P}_e(\Sigma,t) = &\int_B \rho \mathbf{b} \cdot \mathbf{v} dv + \int_{\partial B} \mathbf{p} \cdot \mathbf{v} da \\ &+ \int_{B'} \rho' \mathbf{b}' \cdot \mathbf{v}' dv' \int_{\partial B'} \mathbf{p}' \cdot \mathbf{v}' da' \end{aligned} \tag{19}$$

$$\mathcal{Q}(\partial\Sigma,t) = \int_B r dv - \int_{\partial B} q da + \int_{B'} r' dv' - \int_{\partial B'} q' da' \tag{20}$$

The energy conservation law for ∂B_c and $\partial B'_c$ reduces to:

$$\int_{\partial B_c} \frac{de_c}{dt} da = \int_{\partial B_c} (\mathbf{p} \cdot \mathbf{v} - q)\, da + \int_{\partial B'_c} (\mathbf{p}' \cdot \mathbf{v}' - q')\, da' \tag{21}$$

Rigorously, $\partial B'_c$ may be split onto two parts $\partial B'_c - \partial B_c^{\perp}$ and $\partial B_c^{\perp}$. This allows us to transfer the calculation of the contact power and the heat flux on ∂B_c. Let us recall the contact power

$$\mathcal{P}_c(\partial B_c,t) \equiv \int_{\partial B_c} \mathbf{p} \cdot \mathbf{v} da + \int_{\partial B'_c} \mathbf{p}' \cdot \mathbf{v}' da' \tag{22}$$

The principle of Action-reaction, the fact that $\mathbf{p}' \equiv 0$ on $\partial B'_c - \partial B_c^{\perp}$, and the equilibrium of moment induce:

$$\mathcal{P}_c(\partial B_c,t) = \int_{\partial B_c} \mathbf{p} \cdot \dot{\mathbf{d}} da \tag{23}$$

The three local forms of the energy conservation hold:

$$\begin{aligned} \rho \dot{e}(M,t) &= \sigma : \mathrm{grad}\mathbf{v}(M,t) + r(M,t) - \mathrm{div}\mathbf{J}_q(M,t) \\ \rho' \dot{e}'(M',t) &= \sigma' : \mathrm{grad}\mathbf{v}'(M',t) + r'(M',t) - \mathrm{div}\mathbf{J}'_q(M',t) \\ \dot{e}_c(M,t) &= \mathbf{p} \cdot \dot{\mathbf{d}}(M,t) - q(M,t) - q'\left(M^{\perp}(M,t),t\right) \end{aligned} \tag{24}$$

4. **For entropy.** As for energy, we assume that the entropy $\mathcal{A} = \mathcal{S}$ is not additive and that there is interfacial entropy density:

$$\mathcal{S}(\Sigma,t) = \int_B \rho s dv + \int_{B'} \rho' s' dv' + \int_{\partial B_c} s_c da \tag{25}$$

The entropy supply includes volume and surface terms :

$$\mathcal{B}(\Sigma,t) = \int_B \frac{r}{\theta} dv + \int_{B'} \frac{r'}{\theta'} dv' \tag{26}$$

$$\mathcal{C}(\partial\Sigma,t) = -\int_{\partial B} \frac{q}{\theta} da - \int_{\partial B'} \frac{q'}{\theta'} da' \tag{27}$$

By applying the entropy inequality for any subsystem of Σ, we obtain for any point of B, B', and $\partial B_c \cap \partial B'_c$ respectively:

$$\begin{aligned}
\rho \dot{s}(M,t) &\geq \frac{r}{\theta}(M,t) - \operatorname{div}\left(\frac{\mathbf{J}_q}{\theta}\right)(M,t) \\
\rho' \dot{s}'(M',t) &\geq \frac{r'}{\theta'}(M',t) - \operatorname{div}\left(\frac{\mathbf{J}'_q}{\theta'}\right)(M',t) \\
\dot{s}_c(M,t) &\geq -\left(\frac{q}{\theta}(M,t) + \frac{q'}{\theta'}((M^{\perp}(M,t),t)\right)
\end{aligned} \tag{28}$$

2.3 Constitutive laws at the interface

Interfacial heat transfer is due to heat generation by friction and/or due to the temperature jump across the interface [10], requiring to take into consideration the principles of thermodynamics [11]. By assuming a rate dependence, generic constitutive functions reduce to [9]:

$$\Im_c = \hat{\Im}_c(d_n, \mathbf{d}_T, \theta, \delta\theta, \dot{d}_n, \dot{\mathbf{d}}_T, \dot{\theta}, \dot{\delta\theta}) \tag{29}$$

Definition 1: (Interfacial free energy) The interfacial free energy $\phi_c(M,t)$ distributed on ∂B_c is defined by $\phi_c \equiv e_c - \theta s_c$. We assume that ϕ_c is a (non differentiable) function of the normal contact gap d_n and the tangential contact gap $\mathbf{d}_T$ and a (differentiable) function of the temperature θ on ∂B_c, of the temperature-gap $\delta\theta$ and their rates.

Theorem 1: Let B and B' be two continua in contact with $\phi_c = \hat{\phi}_c(d_n, \mathbf{d}_T, \theta, \delta\theta, \dot{d}_n, \dot{\mathbf{d}}_T, \dot{\theta}, \dot{\delta\theta})$. Assume that the constitutive functions are not dependent on the second-order time derivatives of $(d_n, \mathbf{d}_T, \theta, \delta\theta)$, then:

$$\phi_c = \hat{\phi}_c(d_n, \mathbf{d}_T, \theta) \qquad q' \frac{\delta\theta}{\theta'} + \mathbf{J}_{\mathbf{d}_T} \cdot \dot{\mathbf{d}}_T \geq 0$$

$$\mathbf{J}_{\mathbf{d}_T} \equiv \mathbf{p}_T - \partial_{\mathbf{d}_T}\phi_c \qquad p_n \in \partial_{d_n}\phi_c \qquad s_c = -\frac{\partial\phi_c}{\partial\theta}$$

Proof. By substituting $\dot{s}_c$ from the above definition and $\dot{e}_c$ from (24), by introducing the temperature-gap, (28) reduces to [12,9]:

$$\mathbf{p}\cdot\dot{\mathbf{d}} - \dot{\phi}_c - \dot{\theta} s_c + \frac{q'}{\theta'}\delta\theta \geq 0$$

By introducing the rate of ϕ_c in the entropy inequality and by splitting the contact power into two parts (normal and tangential), we obtain:

$$\begin{aligned}
&(p_n - \partial_{d_n}\phi_c)\dot{d}_n + (\mathbf{p}_T - \partial_{\mathbf{d}_T}\phi_c)\cdot\dot{\mathbf{d}}_T - \left(s_c + \frac{\partial\phi_c}{\partial\theta}\right)\dot{\theta} + \frac{q'}{\theta'}\delta\theta \\
&-\frac{\partial\phi_c}{\partial\delta\theta}\dot{\delta\theta} - (\partial_{\dot{d}_n}\phi_c)\ddot{d}_n - (\partial_{\dot{\mathbf{d}}_T}\phi_c)\ddot{\mathbf{d}}_T - \frac{\partial\phi_c}{\partial\dot{\theta}}\ddot{\theta} - \frac{\partial\phi_c}{\partial\dot{\delta\theta}}\ddot{\delta\theta} \geq 0
\end{aligned} \tag{30}$$

Following Coleman and Noll method [9] we consider constitutive functions independent of $\ddot{d}_n$, $\ddot{\mathbf{d}}_T$, $\ddot{\theta}$, and $\ddot{\delta\theta}$. We can arbitrarily choose second derivatives at the instant t^+. To satisfy (30), it is necessary for second order derivative coefficients to vanish:

$$\partial_{\dot{d}_n}\phi_c = 0 \qquad \partial_{\dot{\mathbf{d}}_T}\phi_c = 0 \qquad \frac{\partial\phi_c}{\partial\dot{\theta}} = 0 \qquad \frac{\partial\phi_c}{\partial\dot{\delta\theta}} = 0 \tag{31}$$

Therefore ϕ_c and s_c, do not depend on either $\dot{\theta}$ or $\dot{\delta\theta}$. We can attribute arbitrary values for $\dot{\theta}$ and $\dot{\delta\theta}$ at t^+ without violating (30). It implies:

$$s_c = -\frac{\partial\phi_c}{\partial\theta} \qquad \frac{\partial\phi_c}{\partial\delta\theta} = 0 \tag{32}$$

1. the interfacial free energy necessarily takes the form of:

$$\phi_c = \hat{\phi}_c(d_n, \mathbf{d}_T, \theta) \tag{33}$$

2. the entropy inequality (30) reduces to:

$$q' \frac{\delta\theta}{\theta'} + J_{d_n}\, \dot{d}_n + \mathbf{J}_{\mathbf{d}_T}\cdot\dot{\mathbf{d}}_T \geq 0 \tag{34}$$

in which:

$$J_{d_n} \equiv p_n - \partial_{d_n}\phi_c \qquad \mathbf{J}_{\mathbf{d}_T} \equiv \mathbf{p}_T - \partial_{\mathbf{d}_T}\phi_c \tag{35}$$

For perfect unilateral contact, the normal relative velocity may take any value and that this must not violate (30). We can deduce:

$$p_n \in \partial_{d_n}\phi_c \qquad s_c = -\frac{\partial\phi_c}{\partial\theta} \qquad q' \frac{\delta\theta}{\theta'} + \mathbf{J}_{\mathbf{d}_T}\cdot\dot{\mathbf{d}}_T \geq 0 \tag{36}$$

The first inclusion is obtained by noticing the inequality $\dot{d}_n \geq 0$. Indeed, we can always conclude that $p_n \in \partial_{d_n}\phi_c$, whatever form of ϕ_c is chosen. It is the indicator function of R_+ with respect to d_n. If the free energy does not depend on $\mathbf{d}_T$, we find the classical unilateral frictional laws [13]. To sum up,

constitutive laws of the thermocontacts may be entirely reconstructed from free energy ϕ_c and quasi potential of dissipation ψ_c [11]:

$$\phi_c = \hat{\phi}_c(d_n, \mathbf{d}_T, \theta) \qquad \psi_c = \hat{\psi}_c\left(\dot{d}_n, \dot{\mathbf{d}}_T, \frac{\delta\theta}{\theta'}\right) \tag{37}$$

2.4 Coulomb dry friction

Usual laws for unilateral contact [13] may be included in the present framework. As a rule we start with local law (one point) and then extend the laws to discrete multidimensional contact, by defining the global displacement vector $\mathcal{U} \equiv (\mathbf{u}(M \in B), \mathbf{u}'(M' \in B'))$.

1. **Unilateral contact.** Unilateral contact laws are summarized by the classical Signorini relationships $d_n \geq 0$, $p_n \leq 0$, and $p_n\, d_n = 0$. Equivalently, multivalued contact law $p_n\,[d_n]$ and its inverse $d_n\,[p_n]$ may be derived from non differentiable two pseudo-potentials:

$$p_n \in \partial \mathbb{I}_{R_+}(d_n) \qquad d_n \in \partial \mathbb{I}_{R_-}(p_n) \tag{38}$$

where the interfacial free energy $\phi_c(d_n) = \mathbb{I}_{R_+}(d_n)$ is the indicator function of real numbers R_+ defined by:

$$\mathbb{I}_{R_+}(d_n) = \begin{cases} 0 & d_n \in R_+ \\ \infty & d_n \notin R_+ \end{cases} \tag{39}$$

$\partial \mathbb{I}_{R_+}(d_n)$ is the sub-differential of $\mathbb{I}_{R_+}(d_n)$ and $\mathbb{I}_{R_-}(p_n)$ its conjugate.

By considering (discrete) global gap vector as it applies in finite element analysis, the unilateral contact laws are (for p contact elements):

$$\mathcal{D}_n(\mathcal{U}) \in \mathbb{R}^p_- \qquad \mathcal{F}_n \in \mathbb{R}^p_+ \qquad \mathcal{D}_n(\mathcal{U}) \cdot \mathcal{F}_n \tag{40}$$

These (in)-equations may be merged into the unilateral contact law [17]:

$$\mathcal{F}_n \in \partial \mathbb{I}_{\mathbb{R}^p_+}[\mathcal{D}_n(\mathcal{U})] \tag{41}$$

2. **Coulomb pure friction.** For pure friction, under a constant pressure $p_n = c^{ste}$, the dissipation potential is $\psi_c = \mathbb{I}^*_{C(p_n)}$. Two cases may occur: stick $\|\mathbf{p}_T\| + \mu p_n < 0$ and slip $\|\mathbf{p}_T\| + \mu p_n = 0$. These two situations may be expressed by means of a slip law, a Coulomb criterion and a complementary condition, μ being the friction coefficient:

$$\dot{\mathbf{d}}_T \|\mathbf{p}_T\| = \|\dot{\mathbf{d}}_T\| \mathbf{p}_T \quad \|\mathbf{p}_T\| + \mu p_n \leq 0 \quad \|\dot{\mathbf{d}}_T\|(\|\mathbf{p}_T\| + \mu p_n) = 0 \tag{42}$$

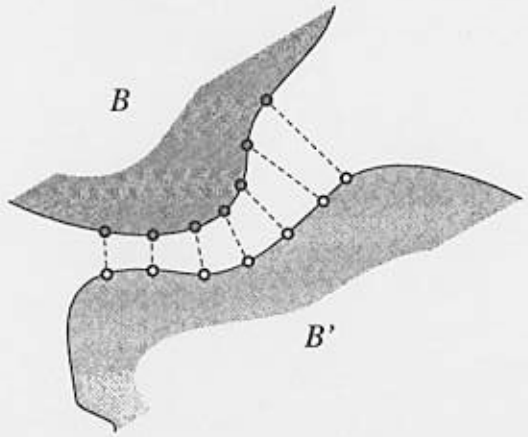

Figure 1. Global contact vectors. After discretization of two solids, the contacting surfaces ∂B_c and $\partial B'_c$ are discretized to define the contact elements (dashed lines). A global gap vector $\mathcal{D}_n$ whose components are the local contact gaps of each contact element $\mathcal{D}_n = (d_n^1, ..., d_n^p)$ where p is the number of contact elements. A global slipping vector is also defined $\mathcal{D}_T = (\mathbf{d}_T^1, ..., \mathbf{d}_T^p)$. Accordingly, global normal contact vector and shear contact vector are defined as $\mathcal{F}_n = (p_n^1, ..., p_n^p)$ and $\mathcal{F}_T = (\mathbf{p}_T^1, ..., \mathbf{p}_T^p)$ respectively.

It is worth to introduce conjugate potentials and their sub-gradients [13]:

$$\mathbf{p}_T \in \partial \mathbb{I}^*_{C(p_n)}\left(\dot{\mathbf{d}}_T\right) \qquad \dot{\mathbf{d}}_T \in \partial \mathbb{I}_{C(p_n)}(\mathbf{p}_T) \tag{43}$$

where $\mathbb{I}^*_{C(p_n)}\left(\dot{\mathbf{d}}_T\right)$ is the Legendre-Fenchel conjugate of $\mathbb{I}_{C(p_n)}(\mathbf{p}_T)$ of the convex disk C of radius $-\mu p_n$ centered at the origin $C = \{\mathbf{p}_T \mid \|\mathbf{p}_T\| + \mu p_n \leq 0, p_n \leq 0\}$. Extending these laws to (discrete) global formulas as previously, the pure friction laws are:

$$\mathcal{F}_T \in \partial \mathbb{I}^*_{C^p}[\mathcal{D}_T(\delta\mathcal{U})] \qquad \mathcal{D}_T(\delta\mathcal{U}) \in \partial \mathbb{I}_{C^p}[\mathcal{F}_T] \tag{44}$$

where $\mathbb{I}^*_{C^p}[\mathcal{D}_T(\delta\mathcal{U})]$ is the conjugate of $\mathbb{I}_{C^p}[\mathcal{D}_T(\delta\mathcal{U})]$.

3. **Unilateral contact with friction.** In unilateral frictional contact, it is known that the normal pressure is coupled with tangential friction. The combination of normal contact and pure friction gives:

$$p_n \in \partial \mathbb{I}_{R_+}(d_n) \qquad \mathbf{p}_T \in \partial \mathbb{I}^*_{C(p_n)}\left(\dot{\mathbf{d}}_T\right) \tag{45}$$

where the domain of friction criterion C depends on p_n. The extension of local laws to (discrete) global formulas as previously gives:

$$\mathcal{F}_n \in \partial \mathbb{I}_{\mathbb{R}_+^p}\left[\mathcal{D}_n\left(\mathcal{U}\right)\right] \qquad \mathcal{F}_T \in \partial \mathbb{I}^{\ *}_{C^p}\left[\mathcal{D}_T\left(\delta\mathcal{U}\right)\right] \tag{46}$$

where each domain C depends on $\mathcal{F}_n$.

4. **Thermocontact with friction**. Heat conduction laws at the interface of two solids were proposed in the past [14]:

$$q' = -\kappa\,\frac{\delta\theta}{\theta'} \qquad \kappa = \hat{\kappa}(p_n)$$

where κ is a heat conduction coefficient at the interface. In the framework of normal dissipation, we can propose the potential [19]:

$$\psi_c = \frac{1}{2}\hat{\kappa}(p_n)\left(\frac{\delta\theta}{\theta'}\right)^2 \qquad q' = \hat{\kappa}(p_n)\,\frac{\delta\theta}{\theta'}$$

For a contact thermomechanics law with friction, we combine the above laws to obtain the interfacial energy and potential dissipation [9]:

$$\begin{aligned}\hat{\phi}_c(d_n) &= \mathbb{I}_{R_+}(d_n)\\ \hat{\psi}_c\left(\dot{\mathrm{d}}_T, \frac{\delta\theta}{\theta'}; p_n\right) &= I^*_{C(p_n)}(\dot{\mathrm{d}}_T) + \frac{1}{2}\hat{\kappa}(p_n)\left(\frac{\delta\theta}{\theta'}\right)^2\end{aligned} \tag{47}$$

3 Numerical Algorithms

We limit to elastic solids subject to conservative external forces and dry frictional contact. Let ψ be the strain energy of B. As an illustration, the constitutive laws of transversely isotropic bone are defined by [15]:

$$\psi = \frac{1}{2}e_1\mathrm{tr}^2\varepsilon + \frac{1}{2}e_2\mathrm{tr}\varepsilon^2 + e_3\mathrm{trM}\varepsilon\mathrm{tr}\varepsilon + e_4\mathrm{trM}\varepsilon^2 + \frac{1}{2}e_5\mathrm{tr}^2\mathbf{M}\varepsilon \tag{48}$$

$$\sigma = -\rho\frac{\partial\psi}{\partial\varepsilon} \qquad \varepsilon = \frac{1}{2}\left(\mathrm{gradu} + \mathrm{gradu}^T\right) \tag{49}$$

in which $\mathbf{M} = \mathbf{m}\otimes\mathbf{m}$ is the structural tensor ($\mathbf{m}$: transverse isotropy direction) and where the elastic coefficients may be related to elastic constants [16]:

$$\begin{aligned}e_1 &= \left(\nu_t + \nu_l^2\frac{E_t}{E_l}\right)\frac{E_t}{\Delta} \qquad e_2 = \frac{E_t}{1+\nu_t}\\ e_3 &= \left(\nu_l - \nu_t + \nu_l\nu_t - \nu_l^2\frac{E_t}{E_l}\right)\frac{E_t}{\Delta} \qquad e_4 = 2\mu_l - \frac{E_t}{1+\nu_t}\\ e_5 &= -4\mu_l + \left(1 - 2\nu_l - 2\nu_l\nu_t - \nu_l^2\frac{E_t}{E_l} + \left(1-\nu_t^2\right)\frac{E_l}{E_t}\right)\frac{E_t}{\Delta}\end{aligned} \tag{50}$$

where $\Delta = \left(1 - \nu_t - 2\nu_l^2\frac{E_t}{E_l}\right)(1+\nu_t)$. The same relations hold for B' but, constitutive equations may be simplified if B' is homogeneous and isotropic.

3.1 Variational formulation

For deriving the (quasistatic) equations governing thermocontact, we proceed step by step. First, for an elastic solid B, the total energy $\Psi(\mathbf{u})$ is equal to the internal energy minus the external potential energies

$$\Psi(\mathbf{u}) = \frac{1}{2}\int_B E^{ijkl}\varepsilon_{ij}(\mathbf{u})\,\varepsilon_{kl}(\mathbf{u})\,dv - \int_B \rho\mathbf{b}\cdot\mathbf{u}dv - \int_{\partial B_p}\mathbf{p}_n\cdot\mathbf{u}da \tag{51}$$

The unconstrained minimization problem would be characterized by the necessary condition (equilibrium equation of B) $\nabla_{\mathbf{w}}\Psi(\mathbf{u}) = 0, \forall\mathbf{w}\in W$, W space of kinematically admissible virtual velocity. Assuming now that B is constrained by unilateral contact on some part of its boundary, we assume dicretized for simplifying (Fig. 1). In presence of inequality constraint $\mathcal{D}_n(\mathcal{U}) \in \mathbb{R}_+^p$, $\mathbb{R}_+^p = R_+\times\ldots\times R_+$ (p-times), minimization problem can be reformulated into a nonconstrained minimization by adding the indicator function to the total energy:

$$\min_{\mathcal{U}}\left\{\Psi(\mathcal{U}) + \mathbb{I}_{\mathbb{R}_+^p}(\mathcal{D}_n)\right\} \tag{52}$$

The solution of the nondifferentiable problem can be characterized by calculating the (sub)-derivative to give (necessarily condition of extremality):

$$0 \in \nabla_{\mathcal{W}}\Psi(\mathcal{U}) + \left[\nabla_{\mathcal{W}}\mathcal{D}_n(\mathcal{U})\right]^T\ \partial\mathbb{I}_{\mathbb{R}_+^p}(\mathcal{D}_n) \qquad \forall\mathcal{W}\in W \tag{53}$$

For two elastic solids subject to conservative external loads, $\mathcal{U}$ includes the two displacement fields of B and B'. The total energy $\Psi \equiv \Psi_B + \Psi'_{B'}$. For solids in unilateral contact, the problem solution becomes:

$$\mathcal{U}^* = \arg\min_{\mathcal{U}}\left\{\Psi(\mathcal{U}) + \mathbb{I}_{\mathbb{R}_+^p}\left[\mathcal{D}_n(\mathcal{U})\right]\right\} \tag{54}$$

where $\mathbb{I}_{\mathbb{R}^p_+}[x]$ is the indicator function of $\mathbb{R}^p_+ = R_+ \times ... \times R_+$. For solids in contact with Coulomb pure friction, the formulation is incremental due to the path dependence,

$$\delta\mathcal{U}^* = \arg\min_{\delta\mathcal{U}^*} \{\Psi(\mathcal{U}+\delta\mathcal{U}) + \mathbb{I}^*_{C^p}[\mathcal{D}_T(\delta\mathcal{U})]\} \tag{55}$$

where $\mathbb{I}^*_C[x]$ is the Fenchel conjugate of $\mathbb{I}_C[x]$ and the set C^p the Cartesian product of p local disks C, with fixed radius. For solids in unilateral contact with Coulomb friction, we have the coupling effects

$$\delta\mathcal{U}^* = \arg\min_{\mathcal{U}}\{\Psi(\mathcal{U}+\delta\mathcal{U}) + \mathbb{I}_{\mathbb{R}^p_+}[\mathcal{D}_n(\mathcal{U}+\delta\mathcal{U})] + \mathbb{I}_{C^p(\mathcal{U}^*)}[\mathcal{D}_T(\delta\mathcal{U})]\} \tag{56}$$

where $C^p(\mathcal{U})$ is the Cartesian product of local disks $C^p(p^*_n)$ whose radius $-p^*_n$ depend on the solution $\mathcal{U}^*$. Therefore, the frictional contact problem is called quasi-optimization problem because $C^p(\mathcal{U}^*)$ depends on solution [8].

3.2 Methods for solving contact mechanics

Two classes of methods are adopted for solving the interface problem.

1. For *penalty method*, $\mathbb{I}_{\mathbb{R}^p_+}[\mathcal{D}_n(\mathcal{U})]$ is approximated by the quadratic function $\frac{r}{2} D^2_{\mathbb{R}^p_+}[\mathcal{D}_n(\mathcal{U})]$, where $D_C(x)$ is the distance between x and C. r is the penalty parameter. This gives the penalized potential to be minimized for unilateral contact:

$$\Pi(\mathcal{U}) \equiv \Psi(\mathcal{U}) + \frac{r}{2} D^2_{\mathbb{R}^p_+}[\mathcal{D}_n(\mathcal{U})] \tag{57}$$

   Solutions of contact carried systematic errors inherent to the method itself [8] (depending on r). In biomechanics where the calculation of variables (micromotions, stresses, and temperature) requires a high precision, it is deemed necessary to develop most accurate computational methods. Another basic motivation for developing Lagrange multiplier methods is to avoid the ill-conditioning associated with the usual penalty methods. r is not a physical parameter.

2. Multiplier methods start by introducing dual variables $\mathcal{F}_n$ (same dimension as $\mathcal{D}_n$). At the equilibrium, dual variables equal the contact reaction at the interface. For *augmented Lagrangian method*, the first step is to define the standard Lagrangian functional:

$$\Pi(\mathcal{U}) \equiv \Psi(\mathcal{U}) + \mathcal{F}_n \cdot \mathcal{D}_n(\mathcal{U}). \tag{58}$$

   An intermediate step is to replace the problem of minimization of $\Psi(\mathcal{U})$ under the nonlinear inequality $\mathcal{D}_n(\mathcal{U}) \in \mathbb{R}^p_+$ by the a mixed $min-max$ problem under linear dual inequality:

$$\min_{\mathcal{U}} \max_{\mathcal{F}_n \leq 0} \{\Psi(\mathcal{U}) + \mathcal{F}_n \cdot \mathcal{D}_n(\mathcal{U})\} \tag{59}$$

   To show this, recall that the indicator function $\mathbb{I}_{\mathbb{R}^p_+}(\mathcal{D}_n)$ is the Legendre-Fenchel conjugate of $\mathbb{I}_{\mathbb{R}^p_-}(\mathcal{F}_n)$ [13]:

$$\mathbb{I}_{\mathbb{R}^p_+}(\mathcal{D}_n) = \sup_{\mathcal{F}_n}\left\{\mathcal{D}_n \cdot \mathcal{F}_n - \mathbb{I}_{\mathbb{R}^p_-}(\mathcal{F}_n)\right\} \tag{60}$$

   In the special case where we deal with indicator function [13], the expression "$\mathcal{D}_n \cdot \mathcal{F}_n - \mathbb{I}_{\mathbb{R}^p_-}(\mathcal{F}_n)$" takes the value $-\infty$ when $\mathcal{F}_n \notin \mathbb{R}^p_-$, then we have the relation:

$$\sup_{\mathcal{F}_n}\left\{\mathcal{D}_n \cdot \mathcal{F}_n - \mathbb{I}_{\mathbb{R}^p_-}(\mathcal{F}_n)\right\} = \sup_{\mathcal{F}_n \in \mathbb{R}^p_-}\{\mathcal{D}_n \cdot \mathcal{F}_n\} \tag{61}$$

   If we work with $\mathbf{R} \cup \infty$ rather than $\mathbf{R}$ the supremum could be replaced by maximum. Therefore, the minimization problem with inequality constraint can be converted into a standard Lagrangian saddle point one:

$$\min_{\mathcal{U}} \max_{\mathcal{F}_n \in \mathbb{R}^p_-} \{\Psi(\mathcal{U}) + \mathcal{F}_n \cdot \mathcal{D}_n(\mathcal{U})\} \tag{62}$$

   Both $\mathcal{D}_n$ and $\mathcal{F}_n$ are unknown variables. The third step consists in relaxing the constraint in the Lagrangian multiplier $\mathcal{F}_n$ by adding a penalization. This gives the augmented Lagrangian functional [8,17]:

$$\Pi_r(\mathcal{U}, \mathcal{F}_n) \equiv \Psi(\mathcal{U}) - \frac{1}{2r}\|\mathcal{F}_n\|^2 + \frac{1}{2r} D^2_{\mathbb{R}^p_+}[\mathcal{S}_n(\mathcal{U})] \tag{63}$$

   in which r is a penalty parameter, $\mathcal{S}_n(\mathcal{U}) \equiv \mathcal{F}_n + r\mathcal{D}_n(\mathcal{U})$ the augmented multiplier, and $D_{\mathbb{R}^p_+}[\mathcal{S}_n]$ the distance between $\mathcal{S}_n$ and $\mathbb{R}^p_+$. The $min-max$ problem with augmented Lagrangian is not constrained:

$$\min_{\mathcal{U}} \max_{\mathcal{F}_n} \{\Pi_r(\mathcal{U}, \mathcal{F}_n)\} \tag{64}$$

   $\Pi_r(\mathcal{U}, \mathcal{F}_n)$ is differentiable with respect to $\mathcal{U}$ and $\mathcal{F}_n$.

3. For unilateral frictional contact, we have the combination of global and incremental formulation due to friction, the augmented Lagrangian functional to be minimized is called quasi-functional since solutions $\mathcal{U}^*$ and $\mathcal{F}^*_n$ appear as arguments through $\mathcal{S}^*_n = \mathcal{F}^*_n + r\mathcal{D}^*_n(\mathcal{U}^*)$:

$$\begin{aligned}\Pi_r(\mathcal{U}, \delta\mathcal{U}, \mathcal{F}_n, \mathcal{F}_T; \mathcal{U}^*, \mathcal{F}^*_n) = {} & \Psi(\mathcal{U}) + \mathcal{F}_n \cdot \mathcal{D}_n(\mathcal{U} + \mathcal{F}_T \cdot \mathcal{D}_T(\delta\mathcal{U})) \\ & + \frac{r}{2}\|\mathcal{D}_n(\mathcal{U})\|^2 - \frac{1}{2r} D^2_{R^p_-}[\mathcal{S}_n(\mathcal{U}, \mathcal{F}_n)] \\ & + \frac{r}{2}\|\mathcal{D}_T(\delta\mathcal{U})\|^2 \\ & - \frac{1}{2r} D^2_{C^p_-(\mathcal{S}_n(\mathcal{U}^*, \mathcal{F}^*_n))}[\mathcal{S}_T(\delta\mathbf{U}, \mathcal{F}_T)]\end{aligned} \tag{65}$$

where $\mathcal{S}_T \equiv \mathcal{F}_T + r\mathcal{D}_T$, and $C^p \equiv C^p\{\mathbb{P}_{R_-^p}[\mathcal{S}_n(\mathcal{U}, \mathcal{F}_n)]\}$

3.3 Methods for solving contact thermomechanics

The variational formulation of contact mechanics is extended to include thermal effects. We have to consider the global displacement vector $\mathcal{U}$ and gap vector $\mathcal{D}$, the global temperature vector $\Theta \equiv (\theta, \theta')$ and temperature gap vector $\mathcal{T} \equiv \theta_0' - \theta_0 + \Delta\theta' - \Delta\theta$. As for frictional contact, we face a quasi-optimization problem.

1. For penalty method, the quasi-functional is proposed as:

$$\Pi(\mathcal{U}, \Theta, \mathcal{U}^*, \Theta^*) = \Psi(\mathcal{U}, \Theta, \mathcal{U}^*, \Theta^*) + \frac{r}{2} D^2_{R_+^p}[\mathcal{D}_n(\mathcal{U})] + \frac{r}{2} h \mathbb{P}_{R_-^p}[\mathcal{D}_n(\mathcal{U}^*)]\ [\mathcal{T}(\Theta)]^2 \quad (66)$$

   We have a lack of symmetry because heating of an elastic body induces significative dilatation but the converse is not true since an elastic deformation does not increase its temperature significantly. Heat conduction through the contact may be proportional to the contact pressure whereas modification of temperature gap does not influence pressure.

2. For augmented Lagrangian method, the quasi-functional includes the dual variable to give for the unilateral contact model:

$$\Pi(\mathcal{U}, \Theta, \mathcal{U}^*, \Theta^*) = \Psi(\mathcal{U}, \Theta, \mathcal{U}^*, \Theta^*) - \frac{1}{2r}\|\mathcal{F}_n\|^2 + \frac{1}{2r} D^2_{R_+^p}[\mathcal{S}_n(\mathcal{U})] + \frac{1}{2} h \mathbb{P}_{R_-^p}[\mathcal{S}_n(\mathcal{U}^*)]\, \mathcal{T}^2(\Theta) \quad (67)$$

   where $\mathcal{S}_n(\mathcal{U}) = \mathcal{F}_n + r\mathcal{D}_n(\mathcal{U})$.

3. For frictional unilateral contact, the augmented Lagrangian quasi-functional holds [18]:

$$\begin{aligned}\Pi_r(\mathcal{U}, \delta\mathcal{U}, \Theta, \mathcal{U}^*, \delta\mathcal{U}^*, \Theta^*, \mathcal{S}_n^*, \mathcal{S}_T^*) = {} & \Psi(\mathcal{U}, \Theta, \mathcal{U}^*, \Theta^*) \\ & + \mathcal{F}_n \cdot \mathcal{D}_n(\mathcal{U}) + \mathcal{F}_T \cdot \mathcal{D}_T(\delta\mathcal{U}) \\ & + \frac{r}{2}|\mathcal{D}_n(\mathcal{U})|^2 - \frac{1}{2r} D^2_{R_-^p}[\mathcal{S}_n(\mathcal{U})] \\ & + \frac{r}{2}\|\mathcal{D}_T(\delta\mathcal{U})\|^2 - \frac{1}{2r} D^2_{C^p(\mathcal{S}_n^*)}[\mathcal{S}_T(\delta\mathcal{U})] \\ & + \frac{1}{2} h \mathbb{P}_{R_-^p}[\mathcal{S}_n(\mathcal{U}^*)]\, \mathcal{T}^2(\Theta) \\ & + \left\{\mathbb{P}_{C^p[\mathcal{S}_T^*]}[\mathcal{S}_T^*] \cdot \mathcal{D}_T^*(\delta\mathcal{U}^*)\right\} \mathcal{T}(\Theta) \quad (68)\end{aligned}$$

   For this latter, the min-max problem of the augmented functional is written as follows:

$$\min_{\mathcal{U},\theta} \max_{\mathcal{F}_n,\mathcal{F}_T} \{\Pi_r(\mathcal{U}, \delta\mathcal{U}, \Theta, \mathcal{U}^*, \delta\mathcal{U}^*, \Theta^*, \mathcal{S}_n^*, \mathcal{S}_T^*)\} \quad (69)$$

   Details of the variational formulations and the generalized jacobian resulting from these $min - max$ problems may be found elsewhere [18].

4 Thermomechanics of the Cemented Hip Stem

4.1 Clinical problems of cemented hip arthroplasty

After cemented total hip replacement, two types of interface failures occur: failure of stem-cement interface as a result of debonding of stem from cement and failure of bone-cement interface as a result of the gradually failure of bone-cement inter-digitation [2,1,19]. Interface failures could have resulted from the occurrence of abnormally high shear and compressive stresses within the cement and excessive debonding and slipping at both stem-cement and bone-cement interfaces. At the bone-cement interface, penetration of the cement into trabecular bone leads to a complex bone-cement interface which also has a tensile and shear interfacial strengths. Despite their geometrical and mechanical complexity, we can assume a unilateral frictional contact for both the bone-cement and cement-prosthesis interfaces. Many factors have been implicated in the distribution of stress and micromotion and among others, friction coefficients at both stem-cement and bone-cement interfaces [20,2], stem stiffness, cement thickness [3,21]. Hence, the goal of this section were to investigate, with the previous models, the effects of the roughness between the bone and the cement, the stem stiffness, and the cement thickness on the cement stress and on the interfacial micromotions after cemented THR. We also investigate the effects of cement thickness on the temperature distribution.

4.2 Finite element model of the cemented hip stem

A collarless, straight, symmetric hip stem with a cement mantle of uniform thickness was digitized and numerically inserted in the reconstructed femur following typical surgical procedure [22] (see Fig. 2). We considered a titanium stem ($Ti6Al4V$) (Young's modulus $E = 110000MPa$, Poisson's ratio: $\nu = 0.3$) and a chromium-cobalt stem (Young's modulus: $E = 200000MPa$, Poisson's ratio: $\nu = 0.3$). For each of them, two interfaces (stem-cement and bone-cement) were modelled as unilateral frictional thermocontact. The Young's modulus of the cement was $2200MPa$. The loading conditions corresponded to the single limb stance situation of a gait cycle. The load bearing

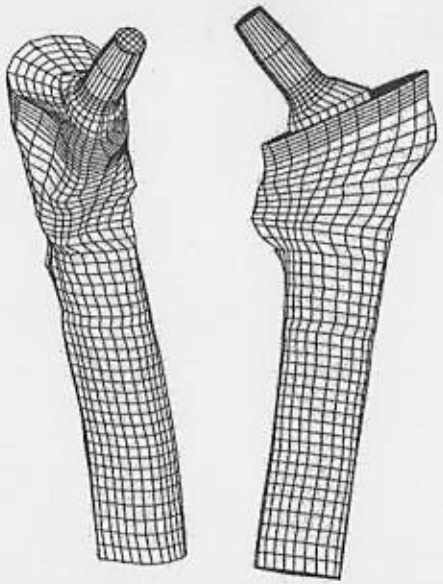

Figure 2. Finite element mesh of the bone-implant system (Anterior-posterior view). The 3D geometry of the femur was reconstructed via Quantitative Computed Tomography.

on the femoral head was simulated with a force of magnitude three times body weight (Patient weight: $600N$) and decomposed into axial, in-plane and out-plane directions [22]. Muscle forces (gluteus minimus, medius, maximus and psoas) were implemented in the model [23,22].

1. The *mechanical analysis* includes three points. First the titanium alloy implant was compared to the chromium-cobalt implant. The cement thickness was set to $4mm$ in this case. The friction coefficients at the bone-cement interface and at the stem-cement interface were set to $\mu_{bc} = 1.0$ and $\mu_{sc} = 0.40$ respectively. Secondly, the sensitivity of the results with respect to the cement thickness was investigated. The cement thicknesses of $2mm$; $3mm$; $4mm$; $5mm$; $7mm$ were used. For regions where the bone thickness did not allow having the prescribed cement thickness, the maximum distance between the implant outer surface and the cortical endosteal femur was used instead. Thirdly, the effects of bone-cement interface rugosity were investigated. To this end, the friction coefficient at the bone-cement interface was set successively: 0.4, 0.6, 0.8 and 1.0. For this example, the thickness of the cement mantle was set $4mm$ [22].

2. For *thermal analysis*, we chose the chromium-cobalt implant inserted with cement of uniform thickness. Two interfaces (stem-cement: $\mu_{sc} = 1.0$; cement-bone: μ_{sc} variable) were considered. The distribution of temperature within the cemented bone-implant system was simulated with different cement thickness: $2mm$, $3mm$, $4mm$ and $5mm$. For the initial and boundary conditions, the temperature of the implant and the bone is initially set as 37°. The temperature of the orthopaedic cement was held uniform and constant at 100°. The outer surface of the femur was kept at the body temperature 37°.

4.3 Micromotions and stresses at the interfaces

1. Titanium alloy versus Cobalt Chromium alloy

   Titanium implant. Distribution of micromotions (debonding and slipping) at the bone-cement interface were calculated. Slipping was higher than $30\mu m$ at the proximal lateral, intermediate medial and distal lateral regions of the bone-cement interface. The peak slipping value was around $67\mu m$. The debonding was in general less than $10\mu m$ over almost the entire region of the interface. Nevertheless, the magnitude could exceed $30\mu m$ in the proximal medial and distal lateral regions (peak: $35\mu m$). At stem-cement interface, slipping exceeded $30\mu m$ over most of the proximal region and then decreased gradually towards the distal part. Concerning the stresses at the bone-cement interface, shear stress exceeded $1.0MPa$ at the proximal lateral, intermediate medial and distal medial regions (peak: $2.4MPa$). Elsewhere, the magnitude remained lower than $0.5MPa$. High compressive stress (peak: $4.4MPa$) occurred in the same locations as the high shear stress (peak: $4.4MPa$). At the stem-cement interface, the peak shear stress was $3.0MPa$ and the peak compressive stress was approximately $7.0MPa$.

   Cobalt chromium implant. At the bone-cement interface, high slipping occurred at the proximal lateral, intermediate medial and distal lateral regions of the interface (Peak values: $68\mu m$). Debonding magnitude was less than $30\mu m$ over the entire interface (Peak value: $28\mu m$). Peak values of micromotions and stresses at stem-cement interface are reported on Table 2 (Peaks debonding : $63\mu m$, slipping: $109\mu m$, compressive stress: $6.6MPa$, shear stress: $2.6MPa$). Peak values of shear and compressive

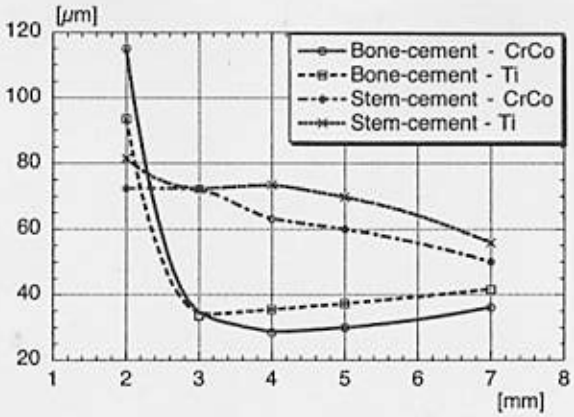

Figure 3. Maximum values of normal relative micromotions $\max_{\partial B_c}\{\mathcal{D}_n\}$ at the bone-cement and cement-stem interfaces related to the thickness of the cement.

stress were higher than $1MPa$ and had nearly the same distribution as for the titanium stem (Peak stress: compressive: $4.2MPa$; shear: $2.5MPa$).

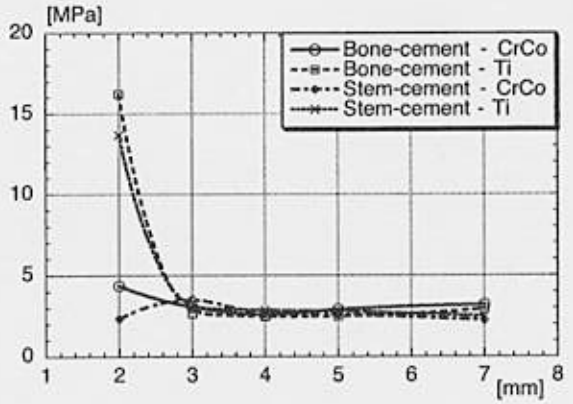

Figure 4. Maximum values of interfacial shear stresses at the bone-cement and cement-stem interfaces related to the thickness of the cement mantle.

2. Influence of the cement thickness

   For both implants, debonding at bone-cement interface increased significantly for a cement $2mm$ thick (cobalt-chromium: $115\mu m$, titanium: $93\mu m$). For a thickness higher than $3mm$, debonding was less than $30\mu m$ over almost the entire interface. At stem-cement interface, maximal debonding decreased slightly with the cement thickness. It was observed that for titanium implant a minimal of debonding peak values ($33\mu m$) occurred when the cement thickness was approximately $3mm$ (Fig. 3) and for chromium cobalt stem, minimum debonding ($28\mu m$) occurred for a cement thickness of $4mm$ (Fig. 3). The cobalt-chromium implant in general had lower debonding than the titanium implant.

   Evolution of slipping at the bone-cement and stem-cement interfaces vs. cement thickness are reported in figure 5. The implant behaviors (titanium and chromium-cobalt) were quite similar. For a cement thickness of less than $3mm$, slipping increased drastically and exceeded $100\mu m$ over the entire bone-cement interface (Titanium: $1650\mu m$, cobalt-chromium $680\mu m$). The peak values of slipping were minimalized when the thickness was $3mm$ ($52\mu m$ for both implants). For a thickness in the range of $3mm, 7mm$, slipping remained constant with highest values occurring in the proximal and distal lateral, and in the medial regions of the bone-cement interface. For thicknesses greater than $7mm$, the peak values of shear micromotions increased to $170\mu m$. In all cases, slipping at the bone-cement interface was greater than slipping at the stem-cement interface.

   Regarding the stress, peak values of shear and compressive stresses at both interfaces (bone-cement and stem-cement) for thickness greater than $3mm$ were not significantly influenced by cement thickness in either implants. For $2mm$ thick layer of cement, abnormally high compressive (Fig. 5) and shear stresses (Fig. 4) were observed at both interfaces for the titanium stem while only a slight increase in stress was noticed for the cobalt-chromium stem. Overall, the shear stress was lower than the compressive stress.

3. Influence of the friction coefficient

   The magnitude of slipping for the friction coefficient at the bone-cement interface was higher than $30\mu m$ for the entire interface for the case of a small friction coefficient ($\mu = 0.4$). The maximal values of slipping were higher for a low friction coefficient and remained nearly constant for higher friction coefficients. Conversely, the debonding was minimal for lower coefficient and maximal for higher coefficient. When the coefficient

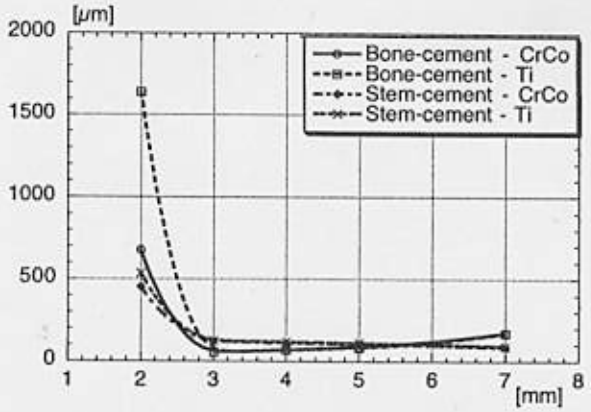

Figure 5. Maximum values of sliding relative micromotions $\max_{\partial B_c}\{\mathcal{D}_T\}$ at the bone-cement and cement-stem interfaces related to the thickness of the cement mantle.

friction of bone-cement interface increased, slipping at the stem-cement interface increased and debonding one decreased (Fig. 6).

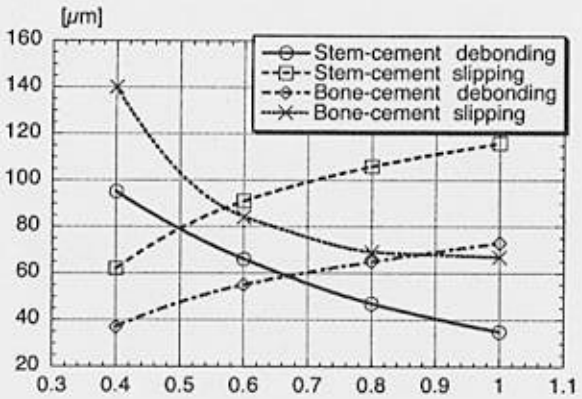

Figure 6. Maximum values of relative micromotions (debonding, sliding) at the bone-cement and cement-stem interfaces related to the friction coefficient.

The compressive stress was minimal for a low friction coefficient ($\mu = 0.4$) and increased gradually with the coefficient while the shear stress remained nearly constant (Fig. 7). Maximal compressive and shear stresses in the cement did not depend significantly on friction coefficient at the bone-cement interface. Bone-cement stresses (compressive and shear) were lower than stem-cement stresses and the shear stress was lower than the compressive stress.

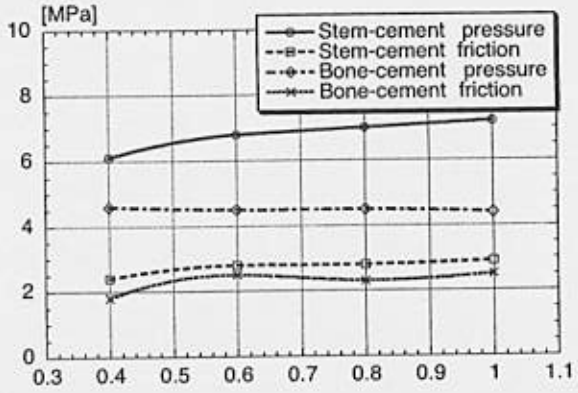

Figure 7. Maximum values of interfacial stresses (pressure, friction) at the bone-cement and cement-stem interfaces related to the friction coefficient.

4.4 Finite element simulation of thermal effects

The distribution of temperature and stress were calculated inside bone, cement, and stem, and at the interfaces (bone-cement and stem-cement) during implantation. Bone, cement and stem properties were taken from [18,22]. Inside structures, peak of temperature was obviously located in the cement. This peak was minimal (76°) when the cement thickness was the lowest $2mm$, and maximal (90°) for a cement mantle of $5mm$ (Fig. 8). At the bone-cement interface, the calculation has shown that temperature increases also with thickness. Stress and temperature were lowest (50°) for a cement mantle thickness of $2mm - 3mm$ and maximal (63°) for a thickness of $5mm$. Moreover, a greater part of the heat generated by polymerization was absorbed by cement and stem. It is attempting to relate the evolution of bone-cement temperature to the probability of late failure at this interface.

The present thermal study has shown that for a cement thickness of $2mm - 3mm$, the peak of temperature inside the bone was minimal. So, even the heat generated by cement may cause bone necrosis in the surround-

ing tissue, an optimal cement thickness might reduce the depth of penetration of this damage inside bone. Such a result should be improved by introducing the kinetics of the cement polymerization [24].

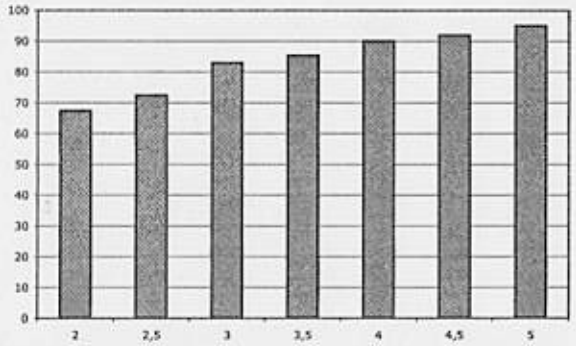

Figure 8. Maximum values of temperature inside the bone-cement-implant system (thickness ranging from $2mm$ to $5mm$).

In addition to temperature field, it was shown that pressure magnitude varies from $+296MPa$ (tensile) and $-97MPa$ (compression). The existence of tensile regions in the vicinity of the interfaces means the occurrence of residual stress when the cement temperature decreases in the course of time. High residual stress near the interfaces is a probable apparition of microcracks density since the mechanical strengths of cement-bone interface, for instance, are respectively $2.25MPa$ and $1.35MPa$ [4].

4.5 Discussion

One should always question if the development of complicated theoretical models and sophisticated numerical algorithms has sense since there are now so many valuable commercial softwares. The following discussion attempts to highlight the usefulness of the previous simulations in the optimization of cement thickness.

1. *Choice of the stem material*

   Comparison of titanium and chromium-cobalt implants (same geometry, friction coefficient, loading condition, and cement thickness) showed that the implant stiffness had no significant effect on micromotion magnitude at the bone-cement interface (Peak: titanium: $67\mu m$, chromium-cobalt: $68\mu m$). The two stems presented comparable lower peak values the shear stress at bone-cement interface (titanium: $2.4MPa$; chromium-cobalt: $2.5MPa$). High stress occurred over the almost the same area for the two implants. However, a fine look at the results pointed out that a $2mm$ cement thickness drastically increased titanium stem stresses but not for chrome-cobalt, which could lead to cement fracture generating in vivo large particulate debris [25].

2. *Optimization of the cement thickness*

   The optimization of the cement thickness during cemented hip arthroplasty remains a challenge for orthopaedic surgeons. Conclusions as to the optimal range of thickness were contradictory. It was shown that a cement mantle thicker than $5mm$ was responsible for the radiolucent lines at the bone-cement interface and a cement mantle lesser than $2mm$ thick induced cement fracture [3]. These findings seemed to be explained numerically by the occurrence of very high shear and compressive stresses [19] which predicted a high risk of cement fracture for a cement less than $3mm$ thick. By accounting for discontinuity at the two interfaces, the present study showed that cement thickness had influence not only on stresses but also on micromotions. A $2mm$ thick layer of cement increased *a*) shear stress in the proximal part and at the tip of the stem and *b*) micromotions over the entire bone-cement interface. These outcomes could be related to local bone necrosis and occurrence of osteolysis in these regions due to the presence of the cemented debris resulting from interfacial shear friction [26]. At the other extreme, thicknesses greater than $7mm$ increased slipping at the bone-cement interface and conformed to experimental results [3]. The present study suggested that an optimum cement thickness was in the range of $3mm - 5mm$ where micromotion peaks were minimal (titanium: slipping $52\mu m$, debonding: $33\mu m$; chromium-cobalt: slipping $52\mu m$, debonding $28\mu m$). Shear stress was also lower when thickness was slightly greater than $3mm$.

   Recent experimental studies have measured the tensile and shear yield stresses $1.35MPa$ and $2.25MPa$. By the way, previous studies on the interface mechanics admitted "penetration error" of the order $\|\mathcal{D}_n\| \simeq 10\mu m$ by using penalty method [7]. In the worst case (cement thickness $e = 2mm$), double penetration at both bone-cement and cement-stem interface gives an error of $2\|\mathcal{D}_n\| \simeq 20\mu m$, which corresponds to a radial cement strain $\varepsilon_c \simeq 10^3 \frac{\mu m}{m}$. This points out the necessity to accurately calculate the variables at the interface, because the comparison of finite element and experimental strains strongly depends on the penalty pa-

rameter. Remembering that bone biology at the bone-cement interface is driven by very small amplitude micromotions [27,28], care should be taken when using non reliable numerical algorithms for solving interfacial thermomechanics.

3. *Choice of the stem surface design*

The choice of surface roughness of the hip stem also remains controversial in orthopaedics. Experimental studies [29] suggested that improving the strength of stem-cement interface should enhance the longevity of the component [30]. However, improved bonding between the cement and the implant might induce early failure of cemented stem [2]. In the same way, numerical simulations showed augmentation of stresses at the bone-cement interface for a fully bonded stem-cement interface compared to partially bonded to the cement [2]. Nonetheless, reduction of stem-cement friction did not decrease shear stresses at the cement-bone interface [19]. Similarly, failure of the bond at the stem-cement interface might initiate the loosening process [31]. This remains a controversial point. By accounting two frictional interfaces, the present example has shown that the decrease of the cement-bone friction coefficient augmented the slipping and decreased the debonding at the bone-cement interface (the stem-cement friction coefficient being maintained constant). In some sense, improvement of the bond at the cement-stem interface significantly increased the relative slipping at the bone-cement interface [22]. Such a phenomenon could be proposed as a biomechanical process promoting early failure at the bone-cement interface [2]. Furthermore, the shear stress magnitude varied slightly with respect to the friction coefficient [19]. The main change was the compressive stress magnitude which was probably due to the hoop effects resulting from the pistoning of the stem in the cement mantle. Such abnormally augmentation of the compressive and hoop stresses certainly induced an overloading of the cement mantle. These results could bring new insight for better understanding biomechanical process of cemented stem failures.

4. *Influence of thermics*

Temperature distribution within the bone-implant system is of central interest for cemented arthroplasty. High temperature may result in thermal injury of surrounding bone. In the same way, the coupling of mechanical and thermal variables is important since the temperature difference at various region arising after orthopaedic cement polymerization induces residual stresses at the interfaces. Namely, the difference between thermal expansion coefficients of the bone, the cement, and the stem are so different and themselves different from the elastic modulus of the stem that stresses are residual concentrated at the interfaces. Experimental measurements have shown significant decreasings of residual stresses on the fracture energies of the bone-cement and cement-stem interfaces [32]. Thermal analysis allows to evaluate temperature distribution during cemented total hip replacement, in order to better understand if the chosen cement mantle thickness presents risks of damage to the tissues surrounding the implant. For thermal aspects, improvements of finite element models by accounting non uniform cement thickness, cement kinetic reaction and other factors [24], should be considered to more accurately evaluate heat generation and temperature distribution. It was also demonstrated that cement cracks resulting from the shrinkage stresses [6] was a most probable source of cement weakness prior to functional loading. Depending on cement temperature and polymerization, stem and bone temperatures, microcrack distribution might be uneven and was denser at the bone-cement interface. In view of all these simplifications, it could be suggested to authors developing finite element interface models to be careful before drawing clinical conclusions whenever interfacial thermomechanics was involved.

Concluding Remarks

Long-term studies of cemented hip arthroplasty have shown that the most frequent cause of failure is the loss of mechanical fixation. Many factors as the bone quality, the implant design and the bone-implant interface are known to influence the quality of fixation of femoral components. Recent investigations have demonstrated that the risk of developing radiolucent lines at the bone-cement interface in the femur was more than 50 percent independently of the stem shape [33]. Evaluation of the bone-implant micromotion and interfacial stress is important for determining the mechanical environment acting on the bone cells [34]. This work is devoted to the developement of thermomechanical models and computational methods to investigate the initial fixation of orthopedic implants. Based on experimental and on clinical studies, [33,27] we assume that radiolucencies at the bone-cement-stem interfaces could be attributed to high shear micromotions. Since the radiolucent line appears for most stem shape designs, a cemented femoral component was chosen to illustrate the developed models by varying different parameters [22]. From biology point of view, radiolucent lines at the bone-cement interface correspond to a fibrous layer, meaning that no close contact forms between the surrounding

bone and the cement mantle. This gap is filled with fibroblasts which may be due to bone necrosis but also potentially by cell death by apoptosis [35] or demineralization [34]. Tissue change often appears after long durations but most probably [33]. Mechanical modelling of cement microcracking behaviour [19] and development of biomechanical models simulating the time evolution of this fibrous tissue layer remain a challenge to bioengineers [36] since all of these phenomena may strongly induce implant instability in the long term.

As with most models, the present one had some limitations. For instance, one should analyze the influence of the stem size and shape, namely the presence of sharp edge, for fixation quality. Important surgical parameters such as a varus orientation of the femoral stem might also influence the non-uniformity of the cement thickness. These problems should be addressed for clinical situations. Among them, the loading case corresponding to single limb stance phase did not constitute the most severe case allowing optimization of cemented femoral component. Use of other loading such as as stair climbing or standing from a chair could give different conclusion. Another limitation was the interface model we used at bone-cement interface. Due to the flow of cement within trabecular bone, the tensile strength at this interface should not be neglected and therefore, a more sophisticated model of stress failure index might be used [19]. Another limitation was the assumption that bone has constant mechanical properties during the course of time. Combination of micromotions and stress analysis with bone density adaptation would be a future extension of the present study. For finite element modelling, there is a controversial assumption about the possibility of debonding at the stem-cement interface [5]. We would like to mention that this interface may be partially or totally bonded immediatly after implantation. Therefore the assumption of totally or partially bonding remains a theoretical approach during the course of time. However, these two extreme hypotheses constitute the two limits to be considered. Varying the friction coefficient at the interfaces [22] or simulating the crack propagation at the interface [19] would be complementary approaches for further investigations.

In summary, contact problems are central to biomechanics of bone-implant interfaces because contact is the principal mean for transfering loads from the implant to bone and vice versa. Thermal stresses due to heat generation and/or heat transfer accross the interface may also decrease the reliability of the cemented implant anchorage. This typically occured for cemented hip replacement. The accuracy of calculation at the interfaces is crucial for reliability of numerical methods and results in this domain. This is demanded by the very high precision of the biological environment at the interfaces: sensitivity relative to the range of shear micromotions for fibrous tissue evolution [36], range of stress stimulus for bone remodelling, range of temperature for bone necrosis. Apart from the unilateral boundary conditions, thermomechanical contact problems present difficulties because of the fact that the extent and the location of the contact area changes during loading and heating. Sometimes, it appears that resolution of computational thermocontact should lie on more fundamental numerical algorithms (consistency) rather than on choosing some pre-implemented solvers and pre-implemented contact elements in pre-existing softwares. In most cases, the use of augmented Lagrangian methods in contact thermomechanics at the bone-implant interface is justified since mixed penalty-duality methods are known to be more robust than primal penalty methods [8,37]. Multiplier methods have the great advantages to give exact solutions of the thermocontact models independently on the algorithm parameters. From mathematics of view (finite dimension), existence theorem was established [37] under most special situations for contact problems with Coulomb friction. In situations where large amplitude slidings are combinated with thermal frictional contact as in head-cup interface after total hip replacement [38], thermomechanics interface models should include large slip capability [17,39] and reformulation of the equilibrium equations should account for the large amplitude motion [40].

Acknowledgments

Scientific advises of Prof A. Curnier (EPF Lausanne) are mostly appreciated during the development of the augmented Lagrangian methods.

References

1. Jasty, M., Maloney, W. J., Bragdon, C. R., O'Connor, D., Haire, T., Harris, W. H., The initiation of failure in cemented femoral components of hip arthroplasties, *J Bone Joint Surg* [Br] **73-B** (1991) pp. 551–8.
2. Gardiner, R. C., Hozack, W. J., Failure of the cement-bone interface: A consequence of strengthning the cement-prosthesis interface, *J Bone Joint Surg* [Br] **76-B** (1994) pp. 49–4.
3. Ebramzadeh, E., Sarmiento, A., McKellop, H. A., Llinas, A., Gogan, W., The cement mantle in total hip arthroplasty: analysis of long-term radiographic results, *J Bone Joint Surg* [Am] **76-A** (1994) pp. 77–11.
4. Mann, K. A., Werner, F. W., Ayers, D. C., Mechanical strength of the cement-bone interface is greater in shear than in tension, *J Biomechanics* **32** (1999) pp. 1251–1254.

5. Stolk, J., Verdonschot, N., Cristofolini, L., Toni, A., Huiskes, R., Finite element and experimental models of cemented hip joint reconstructions can produce similar bone and cement strains in pre-clinical tests, *J Biomechanics* **35** (2002) pp. 499–510.
6. Orr, J. F., Dunne, N. J., Quinn, J. C. Shrinkage stresses in bone cement, *Biomaterials* **24** (2003) pp. 2933–2940.
7. Viceconti, M., Muccini, R., Bernakiewicz, M., Baleani, M., Cristofolini, L., Large-sliding contact elements accurately predict levels of bone-implant micromotion relevant to osseointegration, *J Biomechanics* **33** (2000) pp. 1611–1618.
8. Alart, P., Curnier, A., A mixed formulation for frictional contact problems prone to Newton like solution methods, *Comp Meth Appl Mech Engng* **93**(3) (1991) pp. 353–375.
9. Ramaniraka, N. A., Rakotomanana, L. R., Models of continuum with microcrack distribution. Math Mech Solids **5** (2000) pp. 301–336.
10. Zmitrowicz, A., A thermodynamical model of contact, friction and wear: III Constitutive equations for friction, wear and frictional heat, *Wear* **114** (1987) pp. 199–201.
11. Rakotomanana, L. R., A geometric approach to thermomechanics of dissipating continua, *Birkhauser*, Boston, (2003).
12. Starmans, F. J. M., Brekelmans, W. A. M., Janssen, J. D., A thermodynamic theory for a restricted class of contact behaviour, *Int J Solids Structures* **26**(11) (1990) pp. 1287–1300.
13. Moreau, J. J., On unilateral constraints, friction, plasticity, In Capriz G, Stampacchia G. eds. New variational techniques in mathematical physics (CIME, II-73, Edizioni Cremonese, Roma) (1974), pp. 175–322.
14. Wriggers, P., Miehe, C., Contact constraints within coupled thermomechanical analysis — A finite element model, *Comp Meth Appl Mech Engng* **94** (1994) pp. 301–319.
15. Rakotomanana, R. L., Curnier, A., leyvraz, P. F., An objective anisotropic elastic plastic model and algorithm applicable to bone mechanics, *Eur J mech A/solids* **10**(3) (1991) pp. 327–342.
16. Rakotomanana, R. L., Leyvraz, P. F., Curnier, A., Heegaard, J. H., Rubin, P. J., A finite element model for evaluation of tibial prosthesis-bone interface in total knee replacement, *J Biomechanics* **25** (1992) pp. 1413–1424.
17. Heegaard, J. H., Curnier, A., An augmented lagrangian method for discrete large-slip contact problems, *Int J Num Methods Eng* **36** (1993) pp. 569–593.
18. Ramaniraka, A. N., Thermomécanique des contacts entre deux solides déformables. PhD thesis disseration, Dept. of Mech Engng, EPF Lausanne, (1997).
19. Verdonschot, N., Huiskes, R., Cement debonding process of total hip arthroplasty stems, *Clin Orthop* **336** (1997) pp. 297–11.
20. Harrigan, T. P., Harris, W. H., A three-dimensional non linear finite element study of the effects of cement-prosthesis debonding in cemented femoral total hip components, *J Biomechanics* **24** (1991) pp. 1047-12.
21. Huiskes, R., The various stress patterns of press-fit, ingrown and cemented femoral stems, *Clin Orthop* **261** (1990) pp. 27–12.
22. Ramaniraka, N. A., Rakotomanana, L. R., Leyvraz, P. F., The fixation of the cemented femoral component: Effects of stem stiffness, cement thickness and roughness of the cement-bone surface, *J Bone Joint Surgery* **82-B**(2) (2000) pp. 297–303.
23. Crownshield, R. D., Brand, R. A., A physiologically based criterion of muscle force prediction in locomotion, *J Biomechanics* **11** (1981) pp. 793–9.
24. Hansen, E., Modelling heat transfer in a bone-cement-prosthesis system, *J Biomechanics* **36** (2003) pp. 787–795.
25. McKellop, H. A., Sarmiento, A., Schwinn, C. P., Ebramzadeh, E., In vivo wear of titanium-alloy hip prostheses, *J Bone Joint Surg* [Am] **72-A** (1990) pp. 512-6.
26. Willert, H. G., Bertram, H., Buchhorn, G. H., Osteolysis in alloarthroplasty of the hip: The role of bone cement fragmentation, *Clin Orthop* **258** (1990) pp. 108–14.
27. Farron, A., Rakotomanana, R. L., Zambelli, P. Y., Leyvraz, P. F., Total knee prosthesis. Clinical and numerical study of micromovements of the tibial implant, *Rev Chir Orthop Reparatrice Appar Mot* **80** (1995) pp. 28–35.
28. Jasty, M., Bragdon, C., Burke, D., O'Connor, D., Lowenstein, J., Harris, W. H., In vivo skeletal responses to porous-surfaced implants subjected to small induced motions, *J Bone Joint Surg* [Am] **79** (1997) pp. 707–714.
29. Bundy, K. J., Penn, R. W., The effect of surface preparation on metal/bone cement interfacial strength, *J Biomed Mater Res* **21** (1987) pp. 773–33.
30. Harris, W. H., Is it advantageous to strengthen the cement-metal interface and use a collar for cemented femoral components of total hip replacement? *Clin Orthop* **285** (1992) pp. 67–6.
31. Mohler, C. G., Callaghan, J. J., Collis, D. K., Johnston, R. C., Early loosening of the femoral component at the cement-prosthesis interface after total hip replacement, *J Bone Joint Surg* [Am] **77-A** (1995) pp. 1315–8.

32. Zor, M., Kucuk, M., Aksoy, S., Residual stress effects on fracture energies of cement-bone and cement-implant interfaces, *Biomaterials* **23** (2002) pp. 1595–1601.
33. Ebramzadeh, E., Normand, P. L., Sangiorgio, S. N., Llinás, A., Gruen, T., McKellop, H. A., Sarmiento, A., Long-term radiographic changes in cemented hip arthroplasty with six designs of femoral components, *Biomaterials* **24** (2003) pp. 3351–3363.
34. Pioletti, D. P., Mueller, J., Rakotomanana, L. R., Corbeil, J., Wild, E., Effect of micro-mechanical stimulations on osteoblasts: Development of a device simulating the mechanical situation at the bone-implant interface, *J Biomechanics* **36** (2003) pp. 131–135.
35. Ciapetti, G., Granchi, D., Savarino, L., Cenni, E., Magrini, E., Baldini, N., Giunti, A., In vitro testing of the potential for orthopedic bone cements to cause apoptosis of osteoblast-like cells, *Biomaterials* **23** (2002) pp. 617–627.
36. Buechler, Ph., Pioletti, D. P., Rakotomanana, L. R., Biphasic constitutive laws for biological interface evolution, *Biomech Model Mechanobiology* **1** (2003) pp. 239–249.
37. Pang, J. S., Stewart, D. E., A unified approach to discrete frictional contact problems, *Int J Eng Science* **37** (2003) pp. 1747–1768.
38. Bergmann, G., Graichen, F., Rohlmann, A., Verdonschot, N., van Lenthe, G. H., Frictional heating of total hip implants. Part 2. Finite element study, *J Biomechanics* **34** (2001) pp. 429–435.
39. Pietrzak, G., Curnier, A., Large deformation frictional contact mechanics: Continuum formulation and augmented Lagrangian treatment, *Comput meth Appl Mech Engng* **177** (1999) pp. 351–381.
40. Buechler, P., Rakotomanana, L., Farron, A., Virtual power based algorithm for decoupling large motions from infinitesimal strains: Application to shoulder joint biomechanics. *Comp Meth Biomech Biomed Eng* **5**(6) (2002) pp. 387–396.

ANALYSIS OF TRANSIENT BLOOD FLOW PASSING THROUGH MECHANICAL HEART VALVES BY LATTICE BOLTZMANN METHODS

ORLANDO PELLICCIONI AND MIGUEL CERROLAZA

Bioengineering Center (CeBio UCV)
Central University of Venezuela, 50.381 Caracas – Venezuela.
E-mail: orlandoCEBIO@cantv.net

MAURO HERRERA

Vargas Hospital of Caracas. Caracas – Venezuela.

In the present work a computational method for the simulation of sanguineous flow based on the Lattice-Boltzmann Method is detailed (LBM). A full bidirectional fluid-structure coupling including opening and closing of the valves effecting the hemodynamical properties of the fluid by transient displacements of the solid-fluid boundaries is considered. In this chapter theoretical bases are considered and described briefly. Results from two and three dimensional analyses are shown for different commercial mechanical heart valves prostheses.

1 Introduction

The dynamic flow behavior of human heart valves has intrigued many investigators including Leonardo da Vinci [1], who described a technique for making a model of the aortic valve. Since Hufnagel's successful implantation of a prosthetic heart valve in a human in 1952 [2], numerous *in vitro* investigations have been conducted to clarify the flow characteristics of artificial heart valves.

Either due to congenital defects, aging, diseased states or to trauma, several components of the cardiovascular system can become abnormal. Typical abnormalities include malfunctioning heart valves, stenosed or dilated arterial segments, loss of normal cardiac contractility or cardiac rhythm disturbances. In such situations, the physician desires to take corrective action with medical therapy or percutaneous mechanical procedures such as angioplasty or valvuloplasty. However, if such corrective actions are not possible, an alternative is to replace the malfunctioning parts with artificial devices. Implanting cardiac pacemakers to maintain cardiac rhythm is one of the most common examples of implanted prosthetic devices.

The favorable results obtained using Heart valve prostheses in humans continue to stimulate not only improvement of existing artificial valves but also development of designs and materials. Experimental and clinical success with prostheses of various types implies that an artificial valve does not need to resemble its biological predecessor.

Computational Bioengineering

Current Trends and Applications

editors

M. Cerrolaza
Universidad Central de Venezuela, Venezuela

M. Doblaré
Instituto de Investigación en Ingeniería de Aragón (I3A), España

G. Martínez
Universidad Central de Venezuela, Venezuela

B. Calvo
Instituto de Investigación en Ingeniería de Aragón (I3A), España

ICP

Imperial College Press